Article:
Shi, L, Mao, X and Jaworski, AJ (2010) Application of planar laser-induced fluorescence measurement techniques to study the heat transfer characteristics of parallel-plate heat exchangers in thermoacoustic devices. Measurement Science and Technology, 21 (11). 11. 115405 - 115405. ISSN 0957-0233

https://doi.org/10.1088/0957-0233/21/11/115405

Application of planar laser induced fluorescence (PLIF) measurement techniques to study heat transfer characteristics of parallel-plate heat exchangers in thermoacoustic devices

Lei SHI, Xiaoan MAO and Artur J. JAWORSKI[1]

School of Mechanical, Aerospace and Civil Engineering, University of Manchester
George Begg Building, Sackville Street, Manchester M13 9PL, United Kingdom

ABSTRACT: This paper describes the development of an experimental arrangement and the application of acetone-based Planar Laser Induced Fluorescence (PLIF) measurement techniques to study the unsteady characteristics of heat transfer processes in the parallel-plate heat exchangers of thermoacoustic devices. The experimental rig is a quarter-wavelength acoustic resonator where a standing wave imposes oscillatory flow conditions. Two mock-up heat exchangers: "hot" and "cold", have their fins kept at constant temperatures by electrical heating and water cooling, respectively. A purpose-designed acetone tracer seeding mechanism is used for PLIF temperature measurement. Acetone concentration is optimised from the viewpoint of PLIF signal intensity. Two-dimensional temperature distributions in the gas surrounding the heat exchanger plates, as a function of phase angle in the acoustic cycle, are obtained. Local and global (instantaneous and cycle-averaged) heat flux values on the fin surface are estimated and used to obtain the dependence of the space-cycle averaged Nusselt vs. Reynolds number. Measurement uncertainties are discussed.

KEYWORDS: Temperature Field, Planar Laser Induced Fluorescence; Thermoacoustic Systems; Oscillatory Flow; Heat Exchangers

1 Introduction

The operation of thermoacoustic devices (engines or refrigerators) relies on very complex fluid flow and energy transfer interactions between an oscillatory compressible flow and a solid material. Here, imposing a temperature gradient along the solid may lead to spontaneous generation of acoustic waves along the body. Conversely, imposing an acoustic field in the vicinity of the solid may create a temperature gradient within it due to "heat pumping" phenomena. The key to these so-called "thermoacoustic effects" [1,2] is the relative phasing between pressure and velocity oscillations, which allows the fluid to undergo a thermodynamic cycle, somewhat similar to the Stirling cycle. These phenomena form a basis for constructing thermoacoustic engines, coolers and heat pumps, whose main advantages include the simplicity of construction and lack of moving parts.

[1] Corresponding author, Tel: +44(0)161 275 4352; Fax: +44(0)161 306 3755; E-mail: a.jaworski@manchester.ac.uk

A simplified schematic of a standing-wave thermoacoustic engine is shown in Fig. 1: a "stack" of parallel plates and adjacent hot and cold plate heat exchangers are placed in an acoustic resonator. In a steady state, having reached the thermoacoustic onset condition, the engine absorbs heat $\dot{Q}_h$ at a high temperature T_h and rejects heat $\dot{Q}_c$ at a low temperature T_c, while in the microscopic sense the thermal energy is continuously transferred along the stack by a hydrodynamic "cascade" of oscillating (and at the same time compressing and expanding) gas parcels as shown on the right. The macroscopic effect of gas oscillations is the resulting acoustic wave (acoustic work, $\dot{W}$), which can be transformed into an electrical power output by an electro-acoustic transducer.

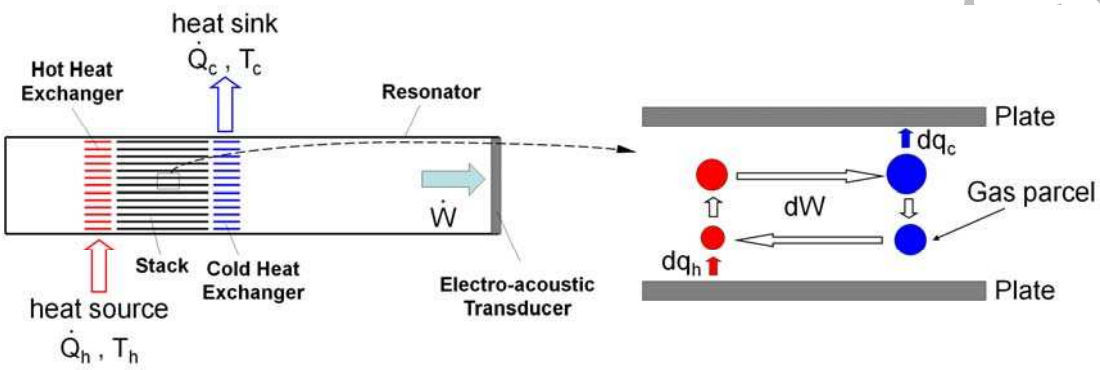

Figure 1 Schematic of a simple standing-wave thermoacoustic engine.

The quantitative description of the fluid flow and heat transfer physics within the stacks is typically based on the linear acoustic theory [1,2], while the design of the heat exchangers is based on relatively simple "rules of thumb" that link the length of the heat exchanger to the displacement amplitude of the fluid parcels, while the plate-to-plate distance is related to the thermal penetration depth: the length-scale that shows the extent of transverse heat transport through the thermal boundary layer within one acoustic cycle. The heat transfer rates are simply predicted by means of standard engineering handbook correlations which are strictly valid only for steady flows.

Unfortunately, in reality the physics of fluid flow and heat transfer processes is much more complex than implied by the simplistic descriptions of the linear acoustic theory and standard steady-flow correlations. Mao and Jaworski [3] investigated the use PIV in oscillating flows around parallel-plate stacks and showed rather complicated processes of turbulence generation, and analyzed the characteristic turbulence length-scales that may be responsible for the heat transfer mechanisms near the internals of thermoacoustic devices. However, only isothermal systems were considered and so no quantitative description of the heat transfer rates was possible.

Current work aims to develop experimental facilities and procedures to implement the full field of view temperature measurement techniques which would become an enabling tool for investigating the heat transfer processes in the critical components of thermoacoustic devices, where potentially

substantial thermodynamic efficiency gains could be achieved. The rationale behind developing such tools is three-fold: Firstly, from the measurement science point of view, to extend the PLIF techniques into new and challenging applications such as thermoacoustic devices; secondly, to gather a substantial set of experimental results to be used in developing appropriate data processing techniques to derive heat transfer rate values, and subsequently to devise reliable heat transfer correlations for oscillatory flows of the type encountered in thermoacoustics; and finally, to provide reliable experimental data for future CFD simulations that could improve the design capabilities of thermoacoustic codes [4]. Using the terminology adopted by MST this work can be classified as "the application of existing techniques in novel situations".

2 Literature review

Previous work on thermal measurements in thermoacoustic/oscillatory systems relied mostly on standard thermocouple techniques, capable only of measuring time-averaged values in selected points, e.g. specific locations within model channels, stacks or heat exchangers. Leong and Jin [5,6] and Jin and Leong [7] investigated heat transfer rates into the channel walls due to an oscillatory flow. The flow conditions were imposed by an oscillating piston-cylinder arrangement, while aluminium foam was used to enhance fluid-to-wall heat transfer. Gopinath and Harder [8] also used thermocouples to investigate the convective heat transfer behaviour from a cylinder in an intense acoustic field, representative of a strong zero-mean oscillatory flow. Such methods are relevant to thermoacoustic systems where stack plates form individual "channels" where heat transfer processes take place, while many heat exchanger designs incorporate various "tube arrangements". Work described in [5-8] led to formulating various Nu vs. Re correlations. Other work by Fu et al. [9] and Ozawa et al. [10, 11] is also worth mentioning.

In thermoacoustics, Paek et al. [12] and Nsofor et al. [13] used thermocouple measurements to study heat transfer in heat exchangers in the oscillatory flow conditions and proposed some correlations involving Nu, Pr and Re numbers. Of course, such studies can only provide measurements of the average heat transfer rates by looking at appropriate energy balances within control volumes defined by researchers. Thus, only "global" correlations can be obtained, where various geometries or flow conditions can be taken into account through comparative studies of a large number of experimental cases. Unfortunately, the changes in heat transfer conditions cannot be linked to specific flow phenomena as no flow processes are observed.

The shortcomings of the time-averaged and "point-wise" thermocouple measurements can be to some extent overcome by cold-wire anemometry, where probes can be traversed within the flow domain of interest. Here a "hot-wire" probe, driven in a constant current mode is used to measure a

time-dependent temperature signal thanks to a high frequency response of the method. Automated traversing and phase-locking techniques can be used to look at temperature profiles across thermal boundary layers in various instances of the acoustic cycle to deduce the local, time-dependent heat transfer rates (and subsequently the appropriately defined Nusselt numbers). Huelsz and Ramos [14] obtained oscillating temperature and the relative phase between temperature and pressure oscillations in acoustic waves, while Mao and Jaworski [15] studied the thermal boundary layer in a channel of a parallel-plate thermoacoustic stack. However, there are many drawbacks: the probes are intrusive and perturb the flow, traversing in the vicinity of internal structures is not easy, while the number of measurement locations required for comprehensive temperature maps is prohibitive.

The shortcomings of thermocouple and "cold-wire" anemometry can be overcome by "full field of view" methods that could capture the unsteady temperature fields around the internal structures (e.g. stacks or heat exchangers) of thermoacoustic devices. However, the only known example seems the work by Wetzel and Herman [16-18], who used holographic interferometry combined with high-speed cinematography to visualize the full temperature field at the edge of a single stack plate placed in an acoustic field. The differences between the heat transfer in oscillatory flows with zero mean velocity and in steady flows have been clearly demonstrated. Similarly, the complex heat transfer mechanisms between the fluid and solid material at the end of a stack plate due to the thermoacoustic effect have been documented. From the measurement science viewpoint, a novel evaluation procedure that accounts for the influence of the acoustic pressure variations on the refractive index was applied to accurately reconstruct the high-speed, two-dimensional oscillating temperature distributions. Nevertheless, it seems that the complexity of the method developed limits its wider practical application as no other works based on the principles described followed.

Current work explores the capabilities of the planar laser-induced fluorescence (PLIF) methods to capture the unsteady temperature fields in thermoacoustic devices due to its non-intrusive nature and a high spatial and temporal resolution. In addition, its use of molecular markers greatly reduces the possibility of the "tracers" lagging behind the fluid (as may be the case in PIV velocity measurements). The physics behind PLIF measurements is well known – cf. [19,20]. Different studies used a variety of molecular tracers as discussed in references [21-34]. Acetone has been one of the popular tracers and gained a wide acceptance after pioneering studies by Thurber et al. [19,20,35,36]. Applications of acetone PLIF (often also combined with other measurement techniques) are discussed in references [37-42].

The choice of acetone in the present study was due to its useful properties: (i) acetone fluorescence in isobaric, isothermal flows is linear with concentration and laser power [43,44]; (ii) acetone

molecules have a broadband excitation spectrum between 225 and 320 nm (flat peak from 270 to 280 nm), which makes them easily excited by conventional high power UV lasers (of a typical wavelength of 266 nm [38]); (iii) depending on the excitation wavelength, the broadband fluorescence between 350-550 nm wavelength exhibits a highly versatile sensitivity vs. temperature which is fundamental for thermometry application; (iv) acetone molecule stays stable and will not disappear below a temperature limit of about 1000 K [45]; (v) acetone molecules have a very high saturating vapour pressure (about 180 Torr at 20°C), which allows an easy seeding into low temperature flow fields; (vi) emission lifetime is short – less than 4 ns [43], which enables "freezing" the temperature images of high-velocity flows; (vii) acetone has low toxicity.

In the context of thermoacoustics, acetone PLIF has an advantage in terms of the dependence of the fluorescence signal on pressure, usually quoted as 5% per MPa for a typical 266 nm excitation wavelength [46]. Therefore the effects of pressure oscillations can be neglected for relatively large acoustic oscillations (e.g. the pressure amplitude of 10 kPa would only result in the maximum oscillation of PLIF signal intensity of 0.05%). For a typical experiment, the overall efficiency of the collection optics, the collection volume and the laser excitation wavelength are constant. Subsequently, at the conditions of constant mole fraction of acetone, the fluorescence signal can be expressed solely as a function of temperature based on relatively simple calibration procedures.

Even though acetone PLIF is a well-established method, it poses an array of new challenges in thermoacoustic applications. In standard applications such as internal combustion engines or jet flows, the temperature fields are investigated within relatively unobstructed imaging domains; and although the temperature distributions may have large temperature gradients (cf. reference [31]), the main focus is the nature of the temperature distribution, not an accurate estimation of the temperature gradient for heat transfer calculations. In the thermoacoustic systems, complex internal solid structures (stacks and heat exchangers) form a set of narrow channels, in which the temperature gradients in very thin thermal boundary layers have to be accurately estimated in order to obtain reliable values of the gas-solid heat transfer rates. Therefore obtaining both a high spatial resolution and good temperature accuracy is much more critical, compared to typical PLIF measurement applications described in the literature.

3 Experimental apparatus and procedures

The acoustic resonator used is geometrically identical to that described by Mao et al. [47], and Mao and Jaworski [3]. However, Perspex sections have been replaced with flanged mild steel sections, while the test section with optical access has been made out of aluminium. The changes were dictated by the introduction of an electrically heated heat exchanger whose high operating

temperatures would render Perspex unsuitable. The use of a heavy metal resonator has also reduced the rig vibration at higher acoustic excitations, while the use of metal flanges allowed a more reliable seal to contain acetone seeding.

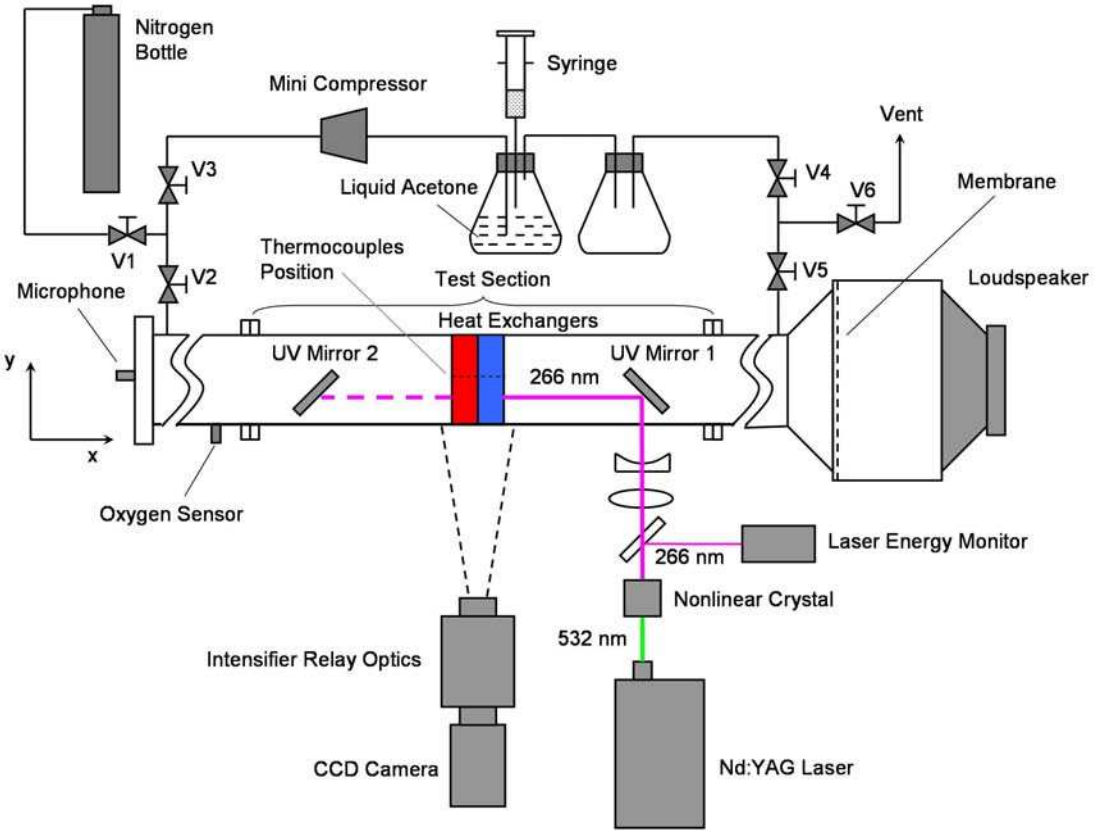

Figure 2 Schematic of the experimental setup.

General schematic of the rig, the seeding arrangement and the PLIF instrumentation are shown in Fig. 2. A 7.4 m long resonator with a square internal cross section of 134 mm by 134 mm is joined with a cube-shaped loudspeaker box using a suitable contraction section. Acoustic excitation (frequency 13.1 Hz in the quarter-wavelength mode) is provided by an 18 inch 600 W loudspeaker (Model PD1850). A Brüel & Kjær microphone (Model 4136) is flush mounted at the rigid end of the resonator to measure the acoustic pressure amplitude for calculating the drive ratio (ratio of oscillating pressure amplitude to the mean pressure in the resonator). The pressure measured by the microphone is also used as a reference signal to trigger PLIF imaging, phase locked to the acoustic cycle – cf. reference [3]. A 0.25 mm thick latex rubber membrane (600 mm x 600 mm) is placed within the loudspeaker box, to separate the loudspeaker from the potentially harmful atmosphere containing acetone vapour. Placing a large membrane at the location where the displacement amplitude is relatively small even at high excitation levels avoids introducing any significant non-linear effects. The mean pressure in the rig is atmospheric.

In the current work the experimental configuration had to be simplified compared to Fig. 1: Firstly,

a pair of heat exchangers is located side-by-side, with no stack (similar to the design in reference [48]). Alternatively, it could be imagined that one of the heat exchangers plays a role of the end of the stack, while the other is treated as an actual heat exchanger. The gas displacement amplitudes are sufficiently small compared to the heat exchanger length to permit such treatment. Secondly, it would not be practically possible to apply high temperature differentials to generate spontaneous acoustic waves (thermoacoustic effect). Instead, the oscillatory flow was imposed by the loudspeaker, while the heat exchangers were placed 4.6 m (about 0.17 of the wavelength) from the end cap of the resonator to mimic an "engine configuration". Furthermore the hot and cold heat exchangers were placed in contact with each other, to avoid creating a gap between them that at this stage could not be illuminated. It should be noted that compared to Fig. 1 above or Fig. 1 in reference [3] the configuration in Fig. 2 is neither an "engine" nor a "refrigerator" – it is designed to mimic engine-like fluid flow and heat transfer processes.

3.1 Heat exchangers

Figure 3a shows the photograph of the hot heat exchanger (HHX, left) and cold heat exchanger (CHX, right) assemblies. Each assembly has ten fins: five are only "dummy plates" (silver-coloured aluminium plates) to provide a uniform porosity, and thus flow conditions, across the cross-section of the resonator; five are "active plates" (golden-coloured brass plates), i.e. have means of controlling their temperature. All plates have a thickness d = 3.2 mm, length l = 35 mm (in the flow direction) and width w = 132 mm (in the transverse direction). The plate spacing is 6 mm.

Each "active" fin in the HHX is made out of a brass plate, with a meandering groove machined in it to accommodate a 600 mm long and 0.062 inch diameter cable heater (Fig 3b left). After fitting the cable heater, a high-temperature epoxy was used to fill in the groove to form a flat surface (not shown). The maximum output power of each cable heater is 240 W. Each "active" CHX fin is made out of a brass plate with a meandering channel for water circulation and a thin brass plate as a cover (Fig. 3b right). The cover is bonded to the fin plate using a soft solder. A water inlet and outlet in each fin are connected to two ends of the water circulation channel by steel tubing (not shown).

The plates are held in position using a series of spacers (6 mm x 10 mm x 50 mm) made out of ceramic material, the whole assembly secured by "supporting pillars". At the rear of the heat exchanger assembly (not shown in Figs. 3a and c) the pillars penetrate all plates, while the spacers are present between all adjacent plates. At the front, the middle channel does not have the ceramic spacer to enable PLIF imaging. Somewhat shorter pillars are used to ensure the integrity of the top and bottom halves of heat exchanger assemblies. The spacers not only ensure the uniform channel height but also prevent thermal distortion of the fins, which was found one of the major problems

during the debugging of the experimental setup.

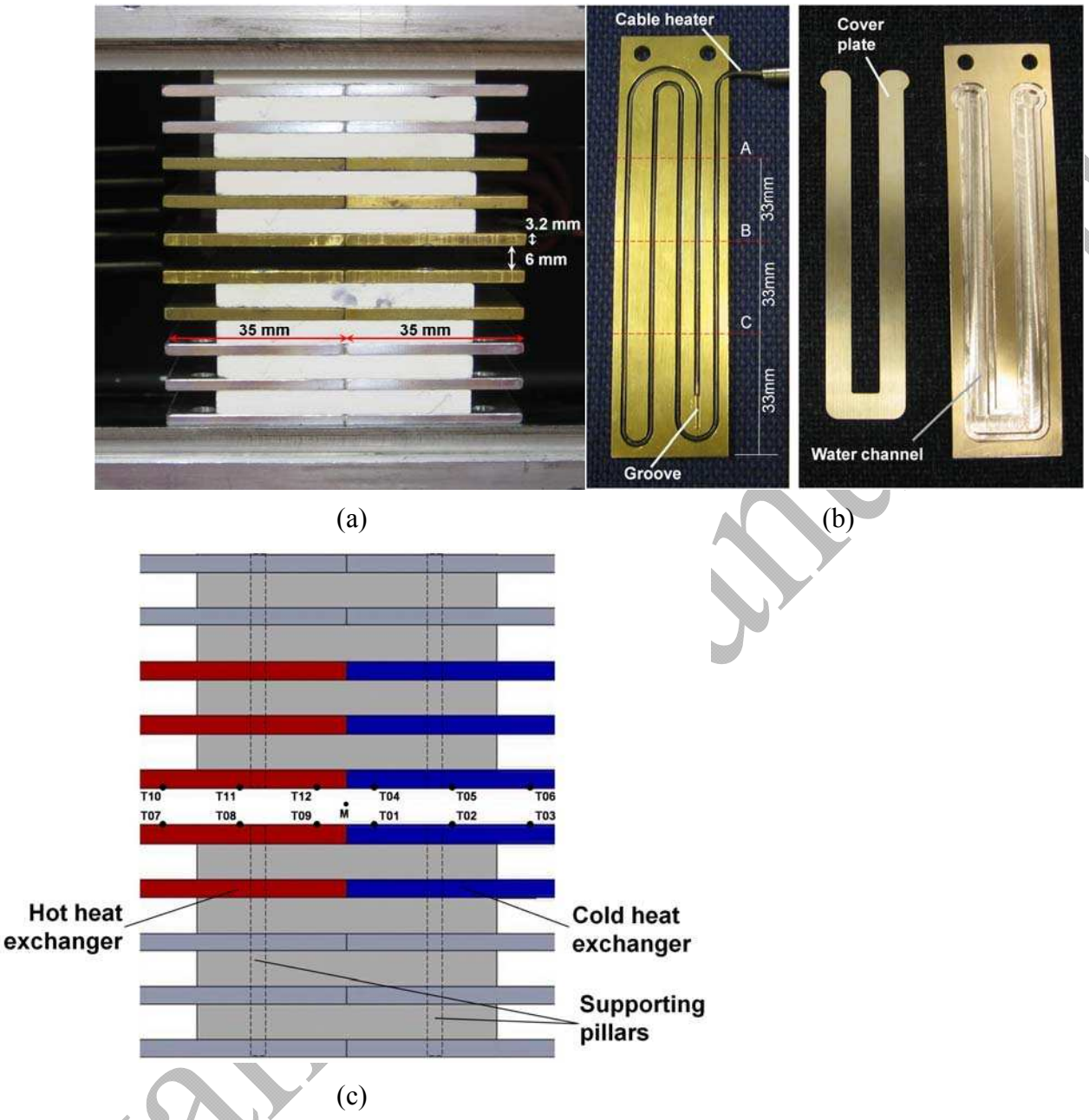

Figure 3 (a) Photograph of the HHX and CHX assemblies; (b) Structure of the "active" hot and cold fins; (c) Schematic showing the location of thermocouples.

Twelve miniature K-type thermocouples (marked "T01" through to "T12"in Fig. 3c) are placed on the surfaces of four heat exchanger fins forming the boundaries of the channel under investigation. Their positions in the span-wise direction are in the centre of the fin as indicated in Fig. 2 (also cross-section B in Fig. 3b). Four thermocouples: "T01" and "T04" on the CHX fins, and "T09" and "T12" on the HHX fins are 3 mm away from the joint between the HHX and CHX. Another four are in the middle of the CHX ("T02" and "T05") and HHX ("T08" and "T11"). The remaining four are placed 3 mm away from the "far end" of the CHX ("T03" and "T06") and the "far end" of the HHX

("T07" and "T10"). One K-type thermocouple of 1 mm diameter was inserted into the investigated channel of the HHX in the direction perpendicular to the laser sheet for temperature calibration of the PLIF system, in such a way that only the "tip" appeared in the laser sheet. After the PLIF calibration (undertaken before every set of experiments) this thermocouple is withdrawn from the laser sheet to avoid any disturbance to the flow field.

A PID temperature controller (Omega Model CN8592) is used to accurately control the temperature at the reference point (here thermocouple "T07" was chosen) to within ±1°C at a preset value (e.g. 200°C). However, the present arrangement of the HHX next to the CHX introduces an unwanted heat conduction flux between the HHX and CHX fins, which makes the surface temperature on the hot and cold fins decrease from left to right. The maximum temperature difference between "T07" and "T09" (or between "T10" and "T12") is around 20°C. Table 1 shows a sample temperature distribution on the fins' surfaces obtained from thermocouples. The span-wise temperature distribution is estimated by distributing thermocouples in three cross-sections of the hot fin: "A", "B" and "C" as shown in Fig. 3b (an analogous measurement is made on the cold fin). However, it is clear from such measurements that the span-wise temperature differences are negligible.

Table 1 Surface temperature of fins measured by twelve thermocouples (gas displacement amplitude 46 mm)

	T10	**T11**	**T12**	**T04**	**T05**	**T06**
Temperature [°C]	200.1	193.7	184.9	44.2	34.4	31
	199.7	192.8	179.8	42.5	33.1	30.4
	T07	**T08**	**T09**	**T01**	**T02**	**T03**

3.2 PLIF system

Temperature field measurements were performed using a PLIF system by LaVision. The laser sheet is generated by an Nd:YAG laser with a UV wavelength of 266nm combined with sheet optics and a divergent lens (cf. Fig. 2). The reading from an energy monitor mounted between the sheet optics and laser head is used for the correction of fluorescence intensity due to the laser energy variation. The averaged laser energy was 54 mJ for a single shot with shot-to-shot energy fluctuations of 0.7%. The fluorescence signal intensity is a linear function of laser energy up to 54 mJ for a single shot.

The laser sheet enters the resonator perpendicularly to its axis through one of two quartz glass windows with 3 mm thickness, is reflected by one of two UV mirrors and becomes parallel to the resonator axis and normal to the surface of the heat exchanger plates. Having two separate laser sheet entry points (to the left and to the right of the heat exchangers) avoids fin shadows in PLIF images. The laser can be simply shifted between the right position corresponding to UV mirror 1 (see Fig. 2) and the left position

corresponding to UV mirror 2 through an automated traversing system. The distance from either of UV mirrors to the joint of HHX and CHX is 300 mm, which is considered to be sufficiently far not to disturb the flow and temperature fields around the heat exchangers. Quartz glass windows are mounted at the locations of the heat exchangers and the two mirrors for taking images of fluorescence, and introducing UV light, respectively. The quartz glass is used for its high transmission of over 90% at 266 nm UV and resulting fluorescence [49].

The laser sheet is 5 mm inwards from the plane marked by "C" in Fig. 3b. A laser sheet position close to the fin end is beneficial from the imaging point of view; the closer it is to the window, the higher the precision of identifying the fin surface in PLIF images. A laser sheet position close to the middle of the fin would ensure as high flow symmetry as possible (except that the mid-point should be avoided due to the flow disturbance from the thermocouples). The chosen sheet position seemed a reasonable trade off between these opposing requirements. From the tests of the fin surface temperatures described in section 3.1, the temperatures measured by twelve thermocouples are considered to represent the surface temperatures of the fins in the laser sheet position.

The PLIF images are captured by an image detection system consisting of LaVision Imager Pro plus camera with a 4 mega-pixel CCD sensor, Intensified Relay Optics (IRO), band pass filter (a broadband pass spectrum extending from 280 to 480 nm, and with flat peak from 350 to 360 nm) for PLIF and macro 105 mm lens with f 2.8. The 2 x 2 hardware "binning" in the camera setup is used for increasing the ratio of PLIF signal to noise. Here, "binning" specifies the collection of a certain number of pixels to a super pixel. Thus, the effective pixels of the CCD sensor become 1024 x 1024 pixels. Images are post processed using LaVision DaVis 7.2 software package. The field of view of the PLIF images for CCD is 65 mm x 65 mm, and the spatial resolution is 0.063 mm per pixel. However, the effective circular view area in IRO is only 56.7% of CCD, which corresponds to around 55 mm in diameter. Therefore, to obtain a full view of temperature field within and around the heat exchangers, three separate views were recorded using an appropriate traversing mechanism, and subsequently "stitched" together in the post-processing stage.

3.3 Acetone seeding system and the optimal concentration

Prior to PLIF measurements, the resonator is homogeneously "seeded" with acetone vapour of a predefined concentration, using a purpose-built seeding system (cf. Fig. 2). It consists of a nitrogen bottle, a gas pump, a syringe (with marked volumes to measure the acetone liquid level), two glass flasks and six valves, all components connected using flexible nylon tubing. A weak acid electrolyte oxygen senor (Envinsci Model Maxtec Max-250) is mounted in the test section to monitor the oxygen concentration. The oxygen sensor output voltage is linear with respect to the oxygen

volumetric concentration. The sensor output varies from about 12.5 mV at 20.9% of oxygen (atmospheric air) to 0.3 mV at 0.5% oxygen concentration.

At standard temperature and pressure (STP) acetone vapour/air mixtures are flammable in the range from 2.6% to 12.8% of acetone vapour by volume [50]. At these conditions, the oxygen concentration in the air-acetone mixture is (1-0.026) x 20.9%=20.4% and (1-0.128) x 20.9%=18.2%, respectively. The ratio of oxygen to acetone vapour is therefore between 1.42 (18.2%/12.8%) and 7.85 (20.4%/2.6%). Therefore, purging the experimental volume with nitrogen until the oxygen percentage drops below 1% (to remove the likelihood of ignition) will allow any acetone vapour concentration above 1%. Detailed operating procedures for the rig are described by Shi et al. [51].

The concentration of acetone vapour is critical for obtaining as high PLIF signal intensity as possible in order to increase the measurement precision [46]. The PLIF signal is proportional to the concentration of acetone vapour (as well as the laser intensity). This means that the high concentration of acetone vapour has a positive effect on obtaining the high PLIF signal intensity. However, while the laser light travels through the fluid a fraction of its energy will also be absorbed by the acetone molecules before reaching the measurement area near the heat exchangers [46]. High concentration of acetone vapour will cause a strong absorption of the laser light. This results in a gradual extinction of the laser beam according to Lambert-Beer's law [46], i.e. an exponential decay of the signal intensity assuming LIF in the linear regime:

$$I(x) = I_0 e^{-\alpha c x} . \quad (1)$$

$I(x)$ and I_0 are the local LIF intensities at an arbitrary position x and $x = 0$, respectively, α is the molar extinction coefficient while c is the acetone concentration. For the fixed position x, one needs an optimal acetone concentration to achieve maximum PLIF signal. Figure 4 shows the relation between the intensity of PLIF signal at point "M" in Fig. 3c and the acetone concentration obtained for the particular experimental arrangement implemented in the current work. The PLIF signal, acquired with the laser energy at 54 mJ for a single shot, was post-processed following procedures described in Section 3.5. The peak intensity corresponds to the optimal acetone concentration of 2%, which was chosen for the PLIF measurements described in this paper.

3.4 Temperature calibration

In acetone-based PLIF the temperature measurement depends on the initial calibration of the LIF signal intensity obtained from PLIF images against the absolute value of temperature obtained for example from a reference thermocouple (cf. section 3.1). During calibration the gas was stationary (no acoustic excitation). For each temperature level (varied from room temperature up to 200ºC) the

setup was allowed to reach a steady state (judged by the thermocouple readings becoming stationary). This approach was chosen to ensure that there are no significant temperature gradients or convective currents in the vicinity of the reference thermocouple. Figure 5 shows the relation between the temperature and true PLIF signal obtained for a sample calibration procedure. Here the curve fitting procedure yielded the following relationship:

$$I = 464.15e^{-0.0056T}. \quad (2)$$

In Fig. 5, the error bars are obtained from the standard deviation of the signal intensity of 100 PLIF images obtained for each temperature point (further described in section 5). It should be noted that in order to obtain a true fluorescence signal for the calibration curve from raw PLIF images, there are relatively involved PLIF image processing procedures required (described in Section 3.5).

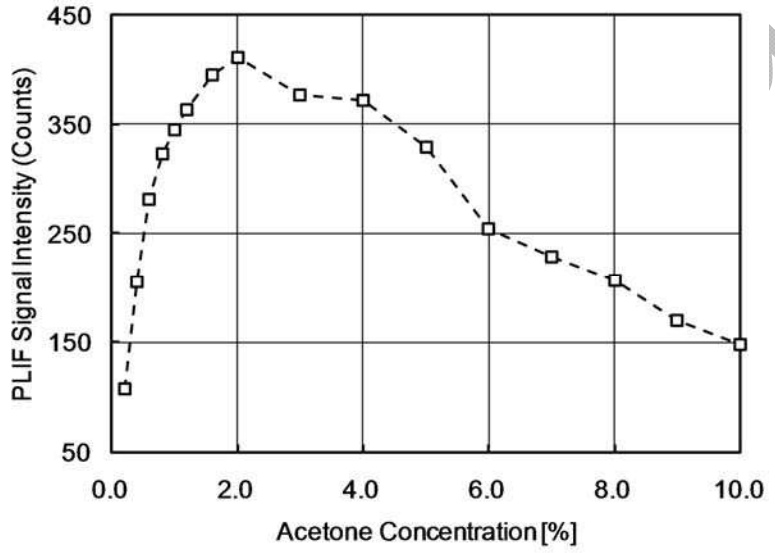

Figure 4 PLIF signal intensity vs. acetone vapour concentration.

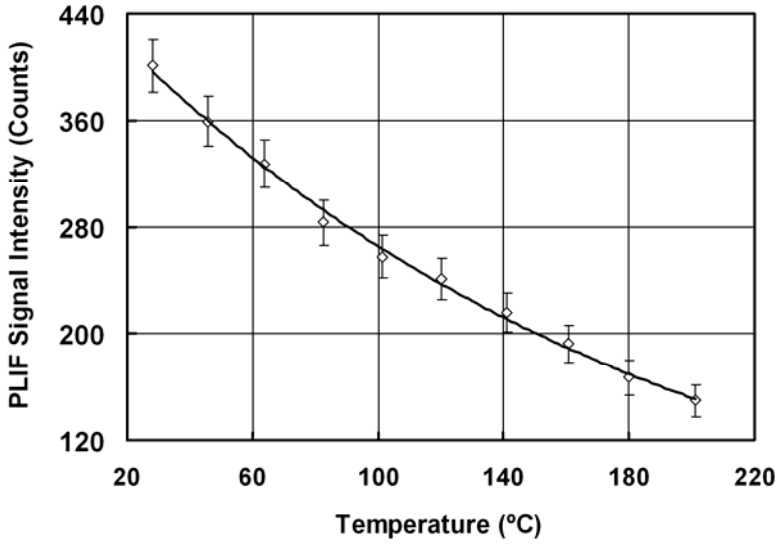

Figure 5 Temperature calibration curve.

For a digital imaging system such as used here, the dominant sources of signal noise are: "shot

noise" (shot-to-shot fluctuation), and "read noise". The latter is also known as the intrinsic camera noise, and consists mainly of dark-current shot noise, "reset noise" and output amplifier noise [52]. The intrinsic camera noise is typically 5 counts (RMS) per pixel for the CCD used. Assuming that the noise sources are uncorrelated, the SNR of a single image can be modelled by [53]:

$$\mathrm{SNR} = \eta N_{pp} G \Big/ \left(\eta N_{pp} \kappa G^2 + N_{cam}^2\right)^{1/2} . \tag{3}$$

In the numerator is the signal (in unit of e^-), $S_e = \eta N_{pp} G$ obtained from the CCD. N_{pp} is the number of photons reaching a single pixel, η is the quantum efficiency of the photodetector and G is the overall electron gain of the intensifier. A gain of 64 was used in the measurements. In the temperature calibration (shown in Fig. 5), the LIF signal recorded is around 400 counts at 20 ºC, and around 150 counts at 200 ºC. The A/D conversion factor of the camera is 0.2 counts/e^-. Thus, the signal given by the CCD, $\eta N_{pp} G$ is around 2000 e^-/pixel at 20 ºC, and around 750 e^-/pixel at 200 ºC. In the denominator of SNR, the shot noise, N_{shot} is:

$$N_{shot} = G\left(\eta \kappa N_{pp}\right)^{1/2} . \tag{4}$$

Here, κ is the total noise factor to quantify the noise induced through the overall gain process between the photocathode and the CCD. It is gain dependent, but normally varies from 1.5 to 2.5. To estimate the maximal shot noise, κ is taken as 2.5. Thus, N_{shot} is estimated to be between 566 e^-/pixel at 20 ºC and 346 e^-/pixel at 200 ºC. N_{cam} is the intrinsic camera noise. It is known that N_{cam} is 25 e^-/pixel for the CCD used. Therefore, SNR of a singe image is between 2.2 at 200 ºC and 3.5 at 20 ºC. If M images (e.g. M = 100) are used for averaging, the SNR of the averaged image is improved by $\sqrt{M}$. Therefore, the SNR of the averaged image of 100 images is between 22 at 200 ºC and 35 at 20 ºC. It can be seen that among these sources of noise, the shot noise is much larger than the noise of camera. By increasing the gain of the intensifier, the signal as well as the first noise term is increased. Overall, the SNR is improved till it reaches the limit, $\left(\eta N_{pp}/\kappa\right)^{1/2}$, when $\eta \kappa N_{pp} G^2 >> N_{cam}^2$.

3.5 Experimental images post-processing and presentation

Figures 4 and 5 show true fluorescence signal after image post-processing procedures from raw PLIF images. These procedures include: (i) "Background subtraction": each image has an offset from the camera's dark current and potentially from the surrounding scattered light. The background signal must be subtracted; (ii) "Sheet image correction": all lasers have a certain spatial profile perpendicular to the beam axis when the laser light is formed into a sheet. All these local laser sheet inhomogeneities will decrease the accuracy of the results. Also the optical components of the detection system will influence the LIF signal due to the local variations of the optical

transmission. These effects are corrected with the sheet correction. The principle behind "Sheet correction" is that the final experimental image is "normalized" by the sheet image; (iii) "Energy correction": an energy monitor is used to monitor the energy variation of the laser beam. This information is used to correct the variations of the fluorescence intensity due to the variations of laser intensity from shot to shot for each PLIF image, when the fluorescence of the tracer is in the regime of linear dependence on the laser energy [46]. There are no further smoothing filters applied to the PLIF images in order to have the genuine fluorescence signal. After the post-processing, the fluorescence images are further converted into the temperature fields shown in Section 4, by using the calibration curve in Fig. 5. The temperature field distributions in Section 4.1 are "stitched" together from the three separate fields of view described in Section 3.2.

4 Experimental results

The results presented here have been taken for four acoustic excitation levels (drive ratios). This has been selected so as to induce four different values of the acoustic displacement at point "M" (cf. Fig. 3c). Table 2 summarises the experimental parameters. Of course, PIV measurements had to be carried out initially in order to measure the acoustic velocity amplitude at point "M". Subsequently, the acoustic displacement, ξ_M could be calculated as $\xi_M = u_M/(2\pi f)$, where f is the acoustic frequency of 13.1 Hz. The PLIF measurements were replicated for the same drive ratios. The temperature settings used in the experiments were 200ºC for thermocouple "T07" (PID controlled), while the resulting "T03" was around 30 ºC (cf. Table 1).

Table 2 Experimental conditions covered by the current study

Drive ratio, Dr [%]	Velocity amplitude at point M, u_M [m/s]	Acoustic displacement, ξ [mm]	Reynolds number based on fin thickness d, Re = $u_M d/\nu$
0.30	1.30	16	250
0.45	1.90	23	357
0.65	2.97	36	535
0.83	3.84	46	702

Measurements were performed for 20 phases within an acoustic cycle as shown in Fig. 6. It shows the reference pressure signal measured by the microphone (used for phase-locking the PLIF system), the reference velocity at point "M" measured by PIV and the calculated reference displacement at point "M". The directions of the velocity and displacement are according to the coordinate system in Fig. 2. When the fluid moves towards the resonator closed end, i.e. the displacement is negative, the absolute pressure at the resonator end is higher than the mean pressure, and the pressure values are positive (cf. Fig. 6). When the fluid moves towards the loudspeaker, i.e. the displacement is positive, the absolute pressure at the resonator end is lower than the mean pressure, and the pressure

is shown as negative. For each phase, 100 frames were taken to calculate the phase-averaged temperature field (a higher number of frames provides negligible accuracy gains).

4.1 Temperature field distributions

Figure 7 shows the temperature fields obtained in 20 phases of the acoustic cycle at Re = 250 (ξ_M = 16 mm). At phase Φ_1, the fluid displacement reaches the maximum negative value (cf. Fig. 6), i.e. the leftmost position in the cycle. The cold gas in the channel formed by the cooled fins (referred to as the "cold channel" hereafter) moves far into the channel formed by the heated fins (referred to as the "hot channel" hereafter) and is heated by the plates. Some part of the hot gas in the hot channel flows out into the open area at the left of the hot fins. Due to the natural convection, the hot gas to the left of the hot fins rises to form a hotter region on the top. After this phase, the gas starts to accelerate to the right until phase Φ_6. At this phase (cf. Fig. 6), the fluid displacement is zero and it is in the so-called "equilibrium position". The cold gas heated by the hot fins partly flows out from the hot channel and moves into the cold channel. Hot gas entering from the open area to the left of the hot fins dominates the left end of the hot channel. After this phase, the gas continues to move to the right. At phase Φ_8, it can be clearly seen that the hot gas partly moves into the cold channel.

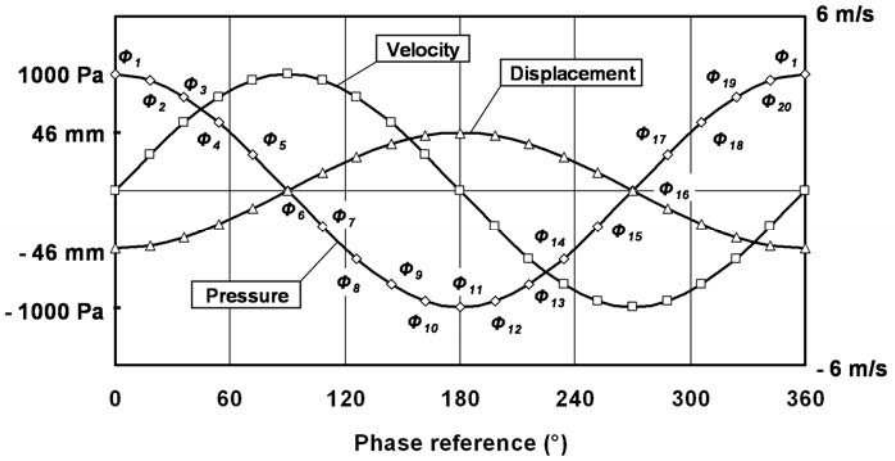

Figure 6 Reference pressure, velocity and displacement for the investigated 20 phases. Gas displacement amplitude is 46 mm. The reference pressure signal was measured at the end of the resonator by the microphone, while the reference velocity at point "M" (cf. Fig. 3c) was measured by PIV. The displacement amplitude at point "M" was calculated as $\xi_M = u_M/(2\pi f)$.

At phase Φ_{11}, the fluid displacement reaches the maximum positive value (cf. Fig. 6), which indicates that the gas reached the rightmost position in the cycle. The hot gas dominates the whole hot channel and partly penetrates into the cold channel. The cold gas in the cold channel partly moves into the open area to the right of the cold fins and mixes with the colder gas in this region. After this phase, the gas starts to move to the left. At phase Φ_{12}, the cold gas in the cold channel gradually moves into the hot channel. The cold gas in the open area to the right of the cold fins partly flows into the cold channel. At phase Φ_{16}, the gas reaches again the "equilibrium position".

The cold gas penetrates as far as possible into the hot channel and the hot gas in the hot channel also migrates into the open area to the left of the hot fins. At phase Φ_{18}, the hot channel is occupied by the cold gas and the hot gas in the hot channel moves further to the left. After this phase, the gas keeps moving to the left until it enters the next acoustic cycle.

Figure 8 shows an analogous set of the temperature field plots at the highest Re investigated: Re = 702 (ξ_M = 46 mm). Clearly, the larger fluid displacement amplitude changes the picture of the temperature fields: the cold gas can penetrate deeper into the hot channel and vice versa. Similarly, the higher velocities cause higher local temperature gradients and lead to higher heat transfer rates (as discussed below). The fluid displacement amplitude of 46 mm is greater than the fin length which causes the hot gas to "overshoot" the CHX and the cold gas to "overshoot" the HHX as can be seen for phase Φ_1 and Φ_{11}.

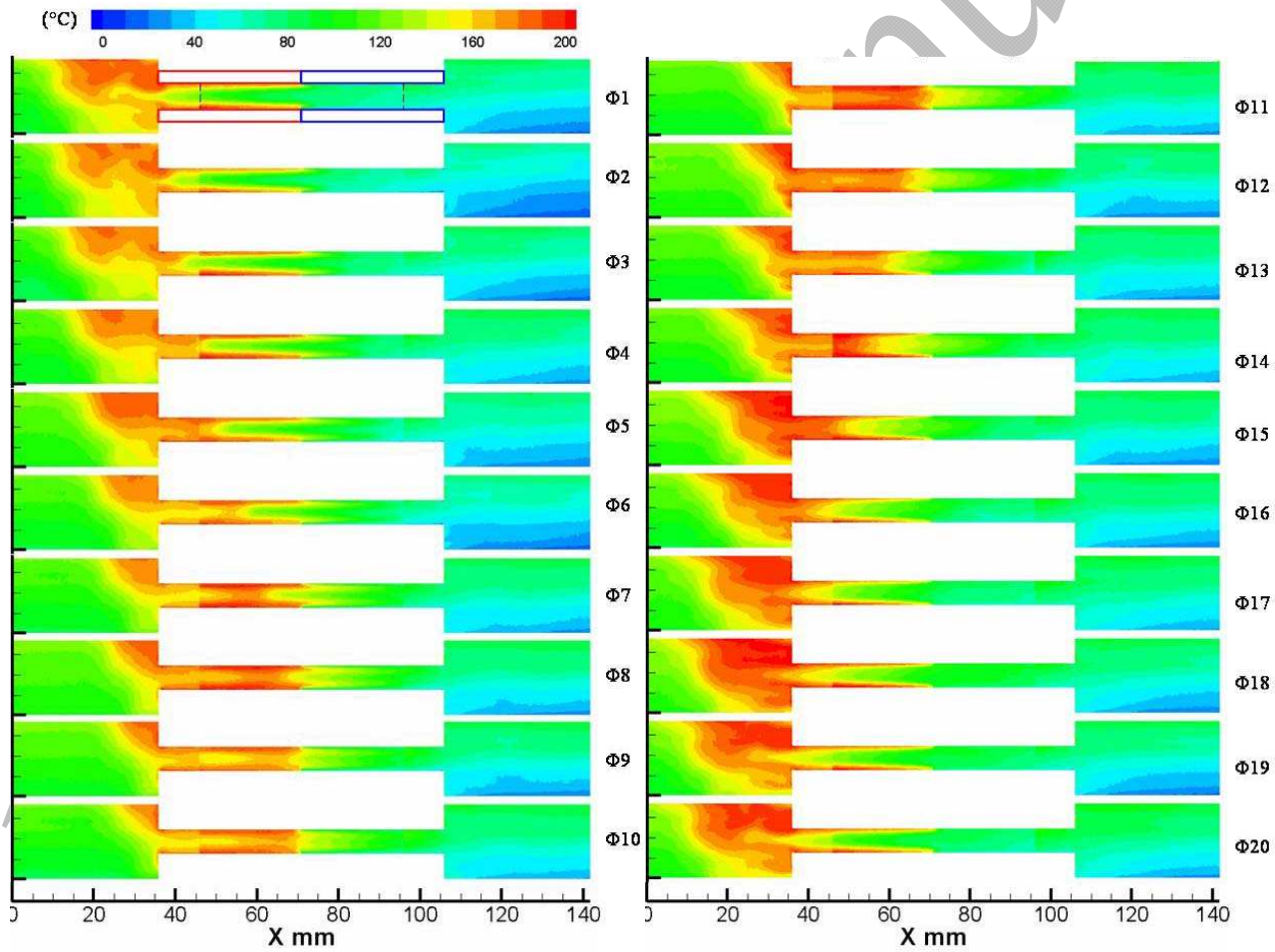

Figure 7 Temperature field distributions for 20 phases within an acoustic cycle at Re = 250. Red rectangles in the first plot mark the heated plates, while blue rectangles mark the cooled plates in the heat exchangers. The black dashed lines mark the "stitching" between the three averaged PLIF images.

It should be noted that slight discontinuities can be seen in Figs. 7 and 8 as a result of "stitching" together three images obtained from consecutive experiments. This is due to the practical implementation of the experiment as well as its overall duration. During the measurements, the

fluorescence images from the middle and right views were obtained with the illumination coming from Mirror 1, while for the left view Mirror 2 was used. Although every effort was made to keep the optical paths the same, there could be differences in the optics and windows in the light path, which may lead to a slightly different level and distribution of the excitation energy from the left and right sides of the heat exchangers. Separate calibrations were impractical because of the thermal inertia of the rig and the time to warm up or cool down the heavy metal resonator. Another cause may be a slight change in acetone concentration during a very long experimental run (3 hours), which may result in temperature discrepancies between neighbouring views.

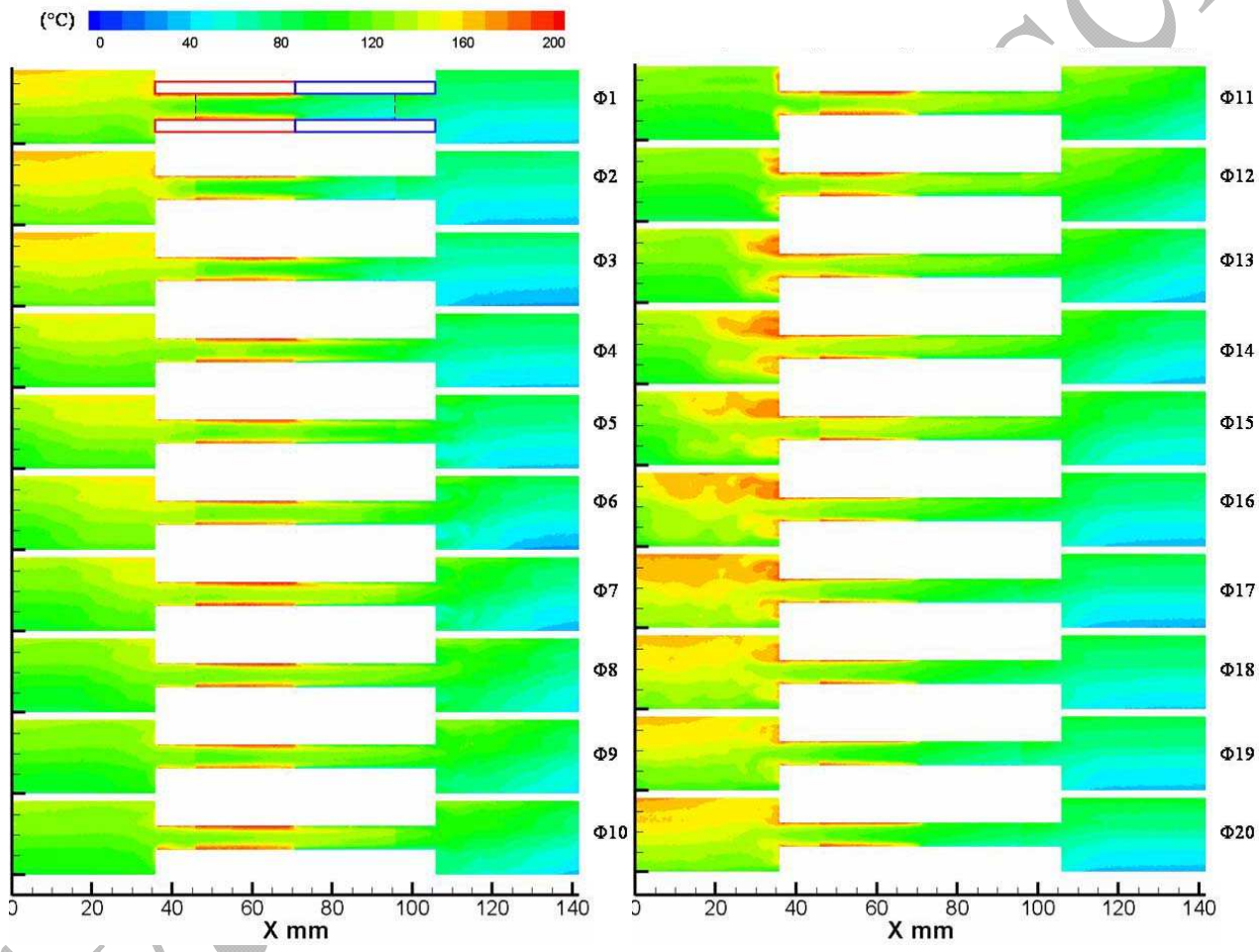

Figure 8 Temperature field distributions for 20 phases within an acoustic cycle at Re = 702.

To further analyse the heat flux, the cross sectional temperature profiles in the hot and cold channel can be investigated at different positions along the flow direction. The respective eight positions in both the hot and cold channels are selected as 1, 5, 10, 15, 20, 25, 30 and 34 mm counting in either direction from the "joint" between the HHX and CHX. Positions 1 and 34 mm are selected to avoid the "joint" and the edges of the hot and cold fins. The "joint" involves a large temperature gradient in both the longitudinal and the transverse direction, thus the measured temperature gradient could introduce a high degree of uncertainty. At the edges of the fins, there is a relatively strong reflection

so that the fluorescence intensity is considered to be unreliable.

The wall temperatures at the 16 positions selected can be obtained by using a linear interpolation of temperature values from the surface mounted thermocouples on the hot and cold fins. As an example, the cross sectional temperature profiles 1 mm away in either direction from the "joint" are shown in Figs. 9a (Re = 250) and 9b (Re= 702) for selected phases in the acoustic cycle (Φ_1, Φ_6, Φ_8, Φ_{12}, Φ_{16} and Φ_{18}). The distance from the fin wall is normalized by the channel width, D = 6 mm. The temperature normalised as follows:

$$\theta = \frac{T_f - T_w}{T_h - T_c}, \qquad (5)$$

where T_f, T_w, T_h and T_c are the local fluid temperature, local wall (fin) temperature, reference hot temperature (here 200ºC), reference cold temperature (here 30ºC), respectively.

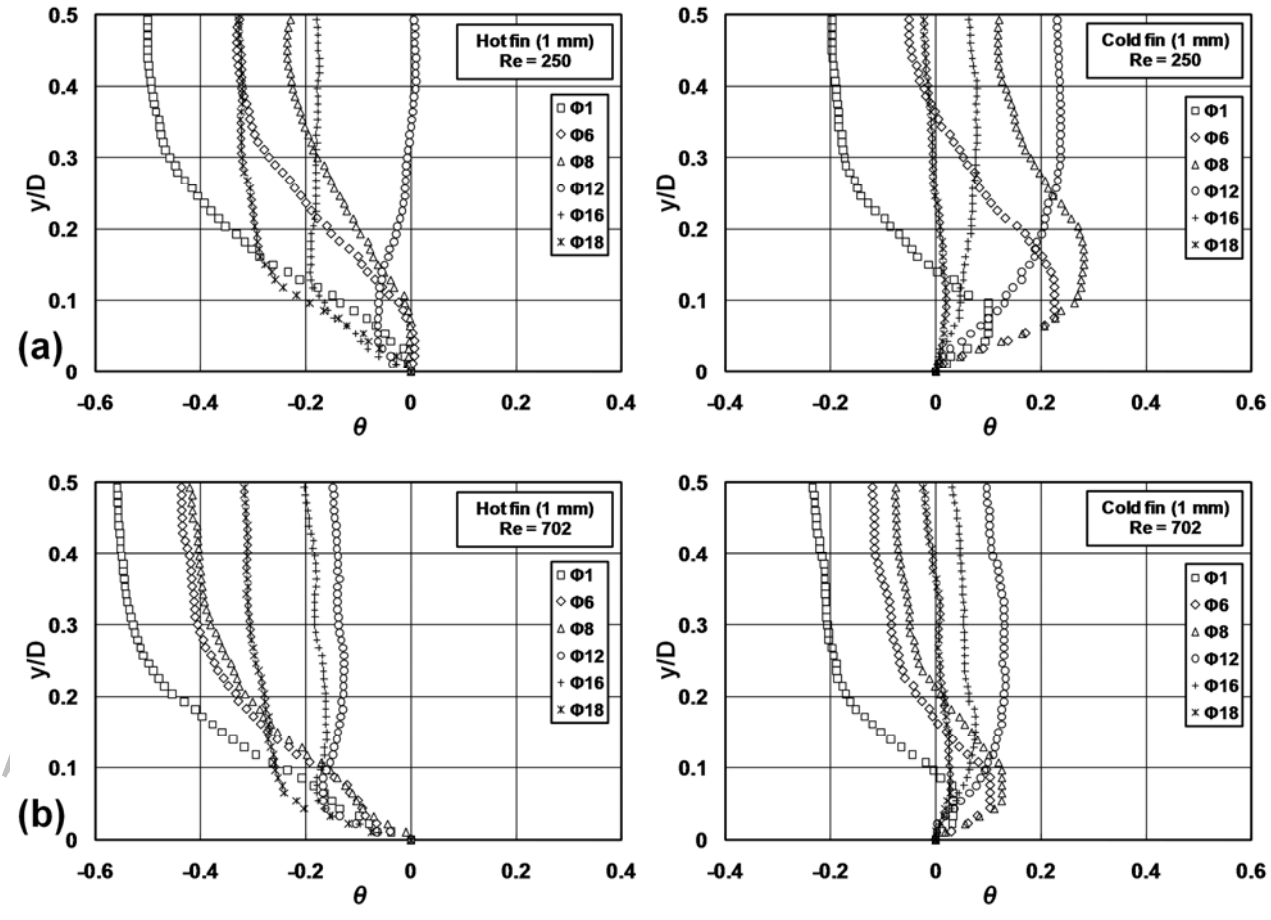

Figure 9 Normalized temperature distributions at selected cross-sections of the hot and cold channels. Graphs on the left are for the position 1 mm from the "joint" above the hot fin. Graphs on the right are for the position 1 mm from the "joint" above the cold fin. Row (a) is for Re = 250. Row (b) is for Re = 702. Only six phases shown.

The temperature profiles in Fig. 9 clearly show the large temperature variations in a very thin layer of gas near the wall. In Fig. 9a, the temperature profiles for all six phases in the hot channel indicate

the heat transfer direction from the plate to the gas, while in the cold channel the heat is always transferred from the gas to the plate. It is also found that in the cold channel, at phase Φ_1, the gas temperature beyond the thin layer near the wall is lower than the wall temperature (a negative θ). It is understood that at this phase the gas is in the leftmost position, and the cold gas from the cold channel moves deep into the hot channel. The colder gas from the right occupies this position for a while so that at phase Φ_6 the temperature in the cold channel centre is still lower than at the wall.

In Fig. 9b, the heat transfer between the gas and the fins in the hot and cold channels is still from the plate to the gas and from the gas to the plate, respectively. The relatively large velocity increases the steepness of temperature profiles. The heat is transferred through the gas near the wall at a higher rate per unit surface area (heat flux density). The large displacement amplitude causes the cold gas to occupy the selected position for a larger part of an acoustic cycle. This is clearly illustrated by the gas temperatures at phase Φ_1, Φ_6, and Φ_8 in the cold channel, which are lower than the wall temperature.

4.2 Heat flux and Nusselt number

The temperature profiles such as those presented in Fig. 9 allow calculating the local, phase-dependent heat fluxes on the fin surface using first principles:

$$q(x,\Phi) = -k\left.\frac{dT(x,y,\Phi)}{dy}\right|_{y=0}, \tag{6}$$

where k is the nitrogen thermal conductivity, which is a function of temperature and can be calculated using a 7^{th} order polynomial [54]. The positive values indicate the heat transfer from the plate to the gas; the negative values indicate the heat transfer from the gas to the plate. The local, phase-dependent, heat fluxes are obtained by linear fitting of temperatures at 6 data points closest to the fin plates along the y direction.

The heat flux $q(x, \Phi)$ is a function of the axial location x and phase Φ. The cycle-averaged local heat flux $q(x)$, the space-averaged phase-dependent heat flux $q(\Phi)$ and the space-cycle averaged heat flux q are defined respectively as,

$$q(x) = \frac{1}{2\pi}\int_0^{2\pi} q(x,\Phi)d\Phi\,, \tag{7}$$

$$q(\Phi) = \frac{1}{l}\int_0^{l} q(x,\Phi)dx\,, \tag{8}$$

$$q = \frac{1}{2\pi}\int_0^{2\pi} q(\Phi)d\Phi = \frac{1}{l}\int_0^{l} q(x)dx = \frac{1}{2\pi l}\int_0^{2\pi}\int_0^{l} q(x,\Phi)dxd\Phi \,. \quad (9)$$

The axial location x includes 16 positions as described in section 4.1; Φ denotes 20 phases in Fig. 6. The integrations in Eqns. (7-9) are performed by using weighted averaging in space and time (phase). Figure 10 shows the space-averaged heat fluxes in the acoustic cycle for four Reynolds numbers investigated. It can be found that the variation of space-averaged heat fluxes has a sinusoidal character as a function of phase. At phase Φ_6 (phase angle 90˚), the heat flux reaches the maximum negative value for Re equal to 250 and 357. It is because at this phase the velocity reaches the maximum, and the gas moves to the right through the "equilibrium position". The hot gas occupies the hot channel and partly penetrates into the cold channel (cf. Fig. 7), which causes the relatively small temperature gradient in the thin thermal boundary layer in the hot channel and a large temperature gradient in the cold channel. Thus, the overall effect is the heat transfer from the gas into the plate.

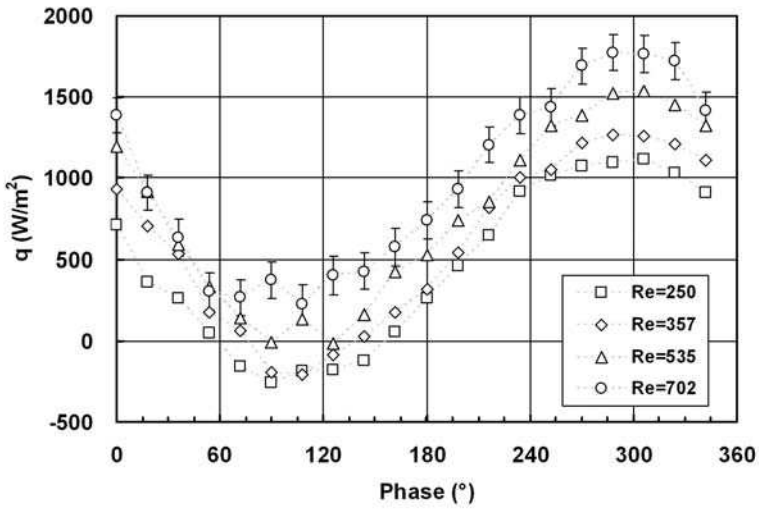

Figure 10 Space-averaged phase-dependent heat fluxes.

For the relatively large values of Re, the high gas displacement causes the gas on the left of the HHX partly reach the cold channel (cf. Fig. 8), which seems to decrease the temperature gradient in the cold channel. The maximum positive heat fluxes appear at about Φ_{16} (phase angle 270˚) when the gas moves to the left through the "equilibrium position". The cold gas dominates the cold channel and penetrates deeply into the hot channel, which causes relatively small temperature gradient in the cold channel and relatively large gradient in the hot channel. The overall effect is the heat transfer from the plates into the gas. These space-averaged phase-dependent heat fluxes increase with Re. This is because of the high velocity and gas displacement amplitudes at higher Re. The high velocity amplitude increases the temperature gradient in the hot and cold channels, while the high gas displacement amplitude increases the heat transfer length in the flow direction.

Figure 11 shows the space-cycle averaged heat flux variation with Re. It can be clearly seen that the heat transfer is from the plate to the gas in the HHX, while the heat transfer is from the gas to the plate in the CHX. The space-cycle averaged heat flux for the HHX is increasing with Re, while for the CHX the maximum heat flux is at Re = 535. At low Re, the gas displacement is less than the length of the HHX and CHX (cf. Fig. 7). The gas heated by the HHX can partly transfer heat to the CHX, while the heated gas at the leftmost end of the HHX cannot exchange heat with the CHX. By the same token, the cold gas at the rightmost end of the CHX cannot exchange heat with the HHX. When Re = 535, the corresponding gas displacement amplitude is 36 mm, which is close to the length of the HHX and CHX (35 mm). It is considered that the gas heated by the HHX can fully transfer heat to the CHX and the cold gas in the CHX can take as much heat as possible heat from the HHX. However, it seems that when the gas displacement amplitude is more than the length of the HHX and CHX (cf. Fig. 8), the colder gas from left of the HHX moves into the CHX but cannot effectively exchange heat with the CHX. Nevertheless the net heat flux between the HHX and CHX increases with Re.

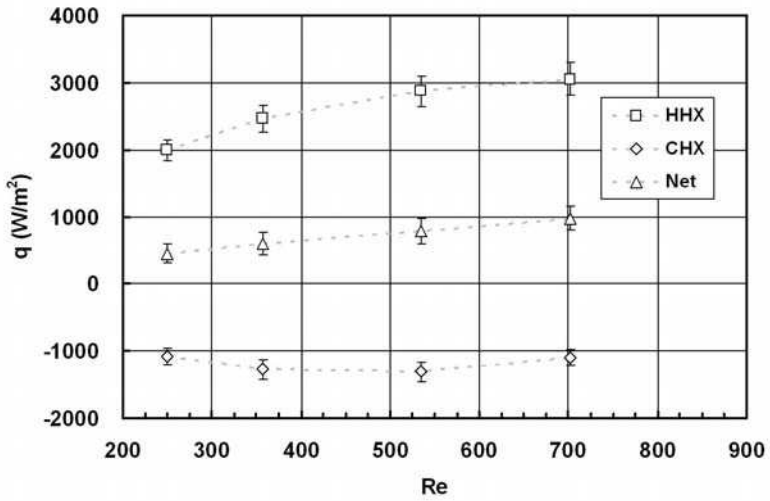

Figure 11 Space-cycle averaged heat flux as a function of Re.

From the local phase-dependent heat flux, the local phase-dependent heat transfer coefficient $h(x,\Phi)$ and the local phase-dependent Nusselt number $\mathrm{Nu}(x, \Phi)$ can be defined as:

$$h(x,\Phi) = \frac{q(x,\Phi)}{\Delta T(x,\Phi)} \tag{10}$$

and

$$\mathrm{Nu}(x,\Phi) = \frac{h(x,\Phi)D}{k}, \tag{11}$$

respectively, where ΔT is the thermal potential for the heat flux. In the oscillatory flow, $\Delta T = T_w - T_i$ is the difference between the wall temperature and the gas temperature at the entrance and exit of the channel or pipe [55]. Here, T_i is selected as the temperature at point "M" in Fig. 3c because this

temperature reflects the interaction between the HHX and CHX. Thus, $\Delta T(x, \Phi) = T_w(x) - T_M(\Phi)$. The space-cycle averaged Nusselt number can be expressed as:

$$\mathrm{Nu} = \frac{1}{2\pi l}\int_0^{2\pi}\int_0^{l}\mathrm{Nu}(x,\Phi)dxd\Phi\,, \tag{12}$$

Figure 12 shows the relation of the space-cycle averaged Nu vs. Re. It is found that the heat transfer correlation for the HHX is different from that for the CHX, i.e. Nu of the HHX is much larger than that of CHX at the same Re. It is reasonable to speculate that heat exchangers with the same configuration (the thickness and length of fin, and the gap between fins) would have the same heat transfer coefficient and thus the same heat transfer correlation, if the operating conditions are appropriately considered in the derivation of the non-dimensional heat transfer correlation. The lack of such agreement suggests that the underlying definition of the heat transfer coefficient does not fully reflect the physics – most likely the tentative selection of the temperature at point M as a reference (by analogy to work [55]) is incorrect. Nevertheless, at the stage of developing the measurement and data processing techniques this issue is not critical and will have to be addressed through further fundamental heat transfer research.

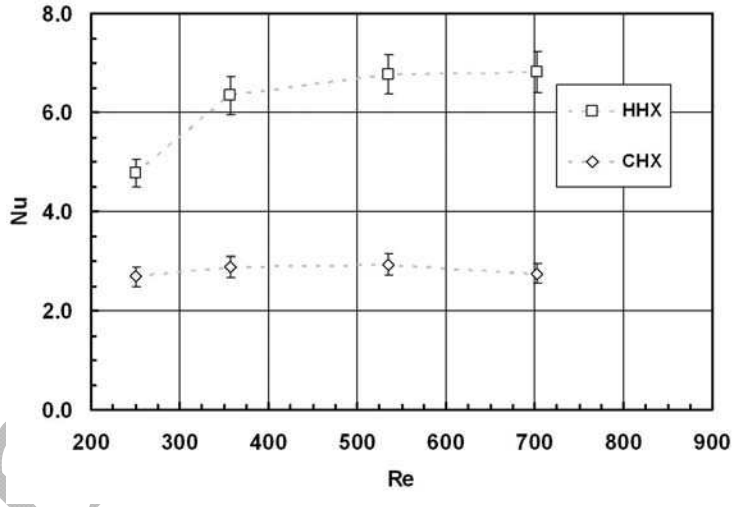

Figure 12 Space-cycle averaged Nu vs. Re.

Figure 12 also shows a similar trend to the heat flux behaviour in Fig. 11, in that Nu for the HHX increases with Re, while Nu for the CHX reaches a maximum at the Re = 535. It is found that the increase of Nu for the HHX becomes weaker for Re over 535 (as though a "saturation" effect took place after the displacement amplitude exceeds the fin length). This agrees well with the thermoacoustic design guidelines explained in Section 1.

5 Uncertainly analysis

As described in section 3.4, the temperature distribution is determined in the following steps:

background subtraction, sheet correction, energy correction and temperature calibration. The precision of any step will contribute to the overall precision of the temperature measurement. According to the theory of error propagation [56], given a function:

$$X = f(A, B, C, ...) , \tag{13}$$

the standard deviation, σ_X, of X can be written as,

$$\sigma_X^2 = (\frac{\partial f}{\partial A}\sigma_A)^2 + (\frac{\partial f}{\partial B}\sigma_B)^2 + (\frac{\partial f}{\partial C}\sigma_C)^2 + ... \tag{14}$$

Here, σ_A, σ_B and σ_C are the standard deviations of A, B and C, respectively.

A general temperature calibration curve can be typically described as [46]:

$$I = ae^{-bT} . \tag{15}$$

Here, a and b are constants determined by the fitting of the calibration curve. Thus, the temperature can be expressed as:

$$T = \frac{\ln a}{b} - \frac{\ln I}{b} . \tag{16}$$

It is indicated that there are a few steps required for correcting the image dark current, laser sheet inhomogeneities, variations of laser energy and so on, before obtaining the true PLIF signals:

$$I = (I_{\exp} - I_{bg}) * C_{ec} * C_{sc} . \tag{17}$$

I_{exp} is the raw PLIF image intensity, I_{bg} is the background image intensity, C_{ec} and C_{sc} are correcting coefficients for the energy and sheet correction. Thus the temperature can be written as,

$$T = \frac{\ln a}{b} - \frac{1}{b}\ln[(I_{\exp} - I_{bg}) * C_{ec} * C_{sc}] . \tag{18}$$

As the laser sheet inhomogeneities and variations of laser energy can be corrected relatively accurately at the post-processing stage through energy correction and sheet correction, the errors caused by them can be practically neglected. A careful analysis indicates that the temperature dependence of the refractive index has a negligible effect on the measurement accuracy.

According to the equation of error propagation, the square of the standard deviation of temperature, σ_T, can be calculated as:

$$\sigma_T^2 = [\frac{\sigma_{I_{\exp}}}{b(I_{\exp} - I_{bg})}]^2 + [\frac{\sigma_{I_{bg}}}{b(I_{\exp} - I_{bg})}]^2 = \frac{1}{b^2(I_{\exp} - I_{bg})^2}(\sigma_{I_{\exp}}^2 + \sigma_{I_{bg}}^2) . \tag{19}$$

Here, $\sigma_{I_{\exp}}$ and $\sigma_{I_{bg}}$ are the standard deviations of the PLIF image and background image, respectively. The standard deviations of the PLIF image correspond to the error bars in Fig. 5. They vary with temperature: a low temperature corresponds to a large standard deviation, while a high

temperature corresponds to a relatively small standard deviation. The standard deviations of the background image have relatively constant values and are originally due to camera dark current (electronic signal determined by the thermal characteristics of the CCD even in the absence of light). The standard deviation of temperature is therefore:

$$\sigma_T = \frac{1}{b(I_{\exp} - I_{bg})}\sqrt{\sigma_{I_{\exp}}^2 + \sigma_{I_{bg}}^2} \quad . \tag{20}$$

Figure 13 shows the changes in standard deviation of temperature measurements with temperature calculated from Eq. (20). It can be found that the standard deviation of temperature increases with temperature. The maximum standard deviation of temperature is around 16 °C at 200 °C, based on averaging of 100 images, i.e. 3.4% (16 K / 473 K) when a relative uncertainty is used. This uncertainty is congruent with literature data concerned with LIF: For example, an uncertainty of 1.8% at 300 K was estimated by Kearney et al. in Rayleigh-Benard convection [40]. An uncertainty of 2.4% at around 350 K, and 4.5% at around 1000K was obtained in a laminar hypersonic flow [57] and 10% between 300 K and 3000 K in shock tunnel flows [58].

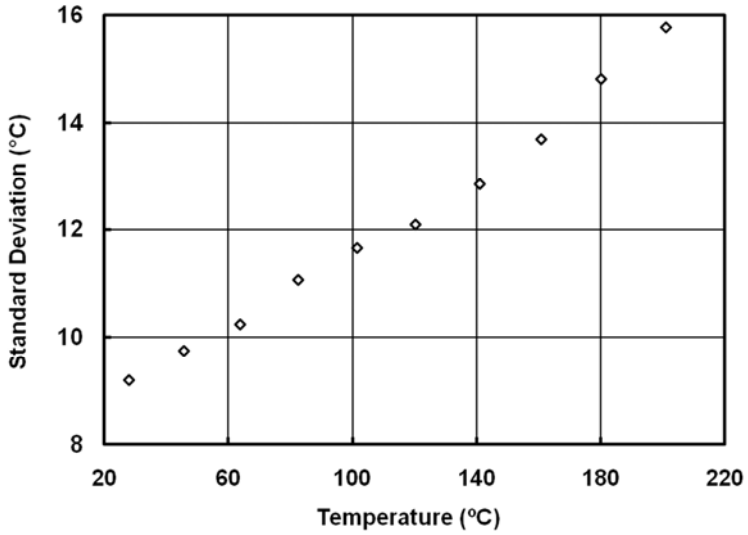

Figure 13 Standard deviations of temperature measurements as a function of temperature.

From the standard deviation of temperature, the standard deviation of local, phase-dependent heat flux, $\sigma_{q(x,\Phi)}$, can be deduced. Since the local, phase-dependent heat flux is obtained by a linear fitting of temperatures at 6 data points near the wall, it can be approximately described as:

$$q(x,\Phi) = -k\left.\frac{dT(x,y,\Phi)}{dy}\right|_{y=0} \approx -k\frac{T_2 - T_1}{\Delta y} \quad . \tag{21}$$

Here, T_1 is the gas temperature closest to the fin wall; T_2 is the gas temperature at one of other 5 data points; Δy is the distance between T_1 and T_2 in y direction. This approximation may exaggerate the uncertainty of local, phase-dependent heat flux because only two data points rather than 6 data points are used. But, the benefit of this approximation is the simplicity of calculation of the

uncertainty of local, phase-dependent heat flux. According to Eq. (14),

$$\sigma_{q(x,\Phi)} = \frac{\sqrt{2}k}{\Delta y}\sigma_T . \tag{22}$$

Uncertainty of space-averaged phase-dependent heat flux, and uncertainty of space-cycle averaged heat flux can be deduced by averaging local, phase-dependent heat flux. They are indicated by the error bars in Figs. 10 and 11, respectively. Combining Eqns. (10), (11) and (22) the uncertainty of the local, phase-dependent Nusselt number, $\sigma_{Nu(x,\Phi)}$, can be expressed as:

$$\sigma_{Nu(x,\Phi)} = \frac{D}{k}\sqrt{\frac{2k^2}{\Delta y^2 \Delta T^2(x,\Phi)} + \frac{q^2(x,\Phi)}{\Delta T^4(x,\Phi)}}\,\sigma_T . \tag{23}$$

Uncertainty of the space-cycle averaged Nu can be reduced by averaging the local, phase-dependent Nu in 20 phases and 8 measured spatial positions. Thus, the maximum uncertainties of the space-cycle average Nu for the HHX and CHX are 0.43 and 0.21, respectively. The uncertainties of the space-cycle average Nu for the HHX and CHX are shown in Fig. 12 for the four values of Re in this study.

6 Conclusion

The focus of this paper is to develop the experimental setup and methodologies for application of acetone-based PLIF for the measurement of time-dependent temperature fields in a challenging environment of oscillatory flows present in the thermoacoustic systems in the vicinity of the parallel-plate heat exchangers. A pair of mock-up heat exchangers was constructed and their thermal performance monitored as a function of acoustic displacement within an acoustically-induced oscillatory flow. However, this study is essentially a test-bed for developing the PLIF methodologies themselves, in particular in terms of the acetone seeding, optimisation of the acetone concentration and the temperature calibration. Furthermore, the obtained time-dependent temperature distributions in an acoustic cycle demonstrate the potential of using the acetone-based PLIF in thermoacoustic systems to obtain temperature gradients and corresponding heat fluxes. This is also indicated by the relatively low uncertainty of Nu obtained from the temperature gradient at the solid-fluid interface. The local temperature distribution profiles in the acoustic cycle and space-averaged phase-dependent heat fluxes reveal the heat transfer variations as a function of phase within the cycle. The space-cycle averaged heat fluxes and changes of Nu vs. Re show that it is possible to monitor (and potentially optimise) the thermal performance of heat exchangers. The technique provides an important foundation for further design studies of heat exchangers in thermoacoustic systems. Future comprehensive heat transfer studies of this type may lead to improved heat transfer correlations or be used as a benchmark for future CFD codes.

Acknowledgments: EPSRC (UK) is acknowledged for funding under grants: GR/S26842/01, GR/T04502/01, GR/T04519/01 and EP/E044379/1 and the European Commission for funding under grant 226415 (THATEA). Dr Z. Yu is thanked for discussions on the heat exchanger build.

References

1. Swift G W 1988 Thermoacoustic engines *The Journal of the Acoustical Society of America* **84**(4) 1145-1180
2. Swift G W 2002 *Thermoacoustics: A Unifying Perspective for Some Engines and Refrigerators* (New York: Acoustical Society of America)
3. Mao X and Jaworski A J 2010 Application of particle image velocimetry measurement techniques to study turbulence characteristics of oscillatory flows around parallel-plate structures in thermoacoustic devices *Measurement and Science Technology* **21**(3)**,** pp 035403
4. Nijeholt à J A L, Tijani M E H and Spoelstra S 2005 Simulation of a travelling-wave thermoacoustic engine using computational fluid dynamics *The Journal of the Acoustical Society of America* **118**(4) 2265-2270
5. Leong K C and Jin L W 2005 An experimental study of heat transfer in oscillating flow through a channel filled with an aluminum foam *International Journal of Heat and Mass Transfer* **48**(2) 243-253
6. Leong K C and Jin L W 2006 Effect of oscillatory frequency on heat transfer in metal foam heat sinks of various pore densities *International Journal of Heat and Mass Transfer* **49**(3-4) 671-681
7. Jin L W and Leong K C 2006 Heat transfer performance of metal foam heat sinks subjected to oscillating flow *IEEE Transactions on Components and Packaging Technologies* **29**(4) 856-863
8. Gopinath A and D R Harder 2000 An experimental study of heat transfer from a cylinder in low-amplitude zero-mean oscillatory flows *International Journal of Heat and Mass Transfer* **43**(4) 505-520
9. Fu H L, Leong K C, Huang X Y and Liu C Y 2001 An experimental study of heat transfer of a porous channel subjected to oscillating flow *Journal of Heat Transfer* **123** 162-170
10. Ozawa M, Shinoki M, Nagoshi K and Serizawa E 2003 Scaling of heat transfer characteristics in an oscillatory flow *Journal of Enhanced Heat Transfer* **10**(3) 275-285
11. Ozawa M and Kawamoto A 2004 Stack temperature distribution in an acoustic-resonance tube *Thermal Science & Engineering* **12**(2) 1-16
12. Paek I, Braun J E and Mongeau L 2005 Characterizing heat transfer coefficients for heat exchangers in standing wave thermoacoustic coolers *The Journal of the Acoustical Society of America* **118**(4) 2271-2280
13. Nsofor E C, Celik S and Wang X 2007 Experimental study on the heat transfer at the heat exchanger of the thermoacoustic refrigerating system *Applied Thermal Engineering* **27**(14-15) 2435-2442
14. Huelsz G. and Ramos E 1998 Temperature measurements inside the oscillatory boundary layer produced by acoustic waves *The Journal of the Acoustical Society of America* **103**(3) 1532-1537
15. Mao X and Jaworski A J 2007 Measurement of thermal boundary layer in a channel of parallel-plate thermoacoustic stack *International Congress of Refrigeration* (Beijing, China)
16. Wetzel M and Herman C 1998 Accurate measurement of high-speed, unsteady temperature fields by holographic interferometry in the presence of periodic pressure variations *Measurement Science and Technology* **9** 939-951
17. Wetzel M and Herman C 2000 Experimental study of thermoacoustic effects on a single plate Part I: Temperature fields *Heat and Mass Transfer* **36**(1) 7-20
18. Wetzel M and Herman C 1999 Experimental study of thermoacoustic effects on a single plate Part II: *Heat transfer Heat and Mass Transfer* **35**(6) 433-441
19. Thurber M C, Grisch F, Kirby B J, Votsmeier M and Hanson R K 1998 Measurements and modeling of acetone laser-induced fluorescence with implications for temperature-imaging diagnos*tics Applied Optics* **37**(21)

4963-4978

20. Thurber M C 1999 Acetone Laser-Induced Fluorescence for Temperature and Multiparameter Imaging in Gaseous Flows *PhD Thesis* Thermophysics Division, Department of Mechanical Engineering, Stanford University, Stanford, California
21. Guibert P, Modica V and Morin C 2006 Influence of pressure, temperature and gas phase composition on biacetyl laser-induced fluorescence *Experiments in Fluids* **40** 245-256
22. Fajardo C M, Smith J D and Sick V 2006 PIV, high-speed PLIF and chemiluminescence imaging for near-spark-plug investigations in IC engines *Journal of Physics: Conference Series* **45** 19-26
23. Giezendanner-thoben R, Meier U, Meier M, and Aigner M 2005 Phase-Locked Temperature Measurements by Two-Line OH PLIF Thermometry of a Self-Excited Combustion Instability in a Gas Turbine Model Combustor *Flow, Turbulence and Combustion* **2005**(75) 317-333
24. Sadanandan R, Stöhr M and Meier W 2008 Simultaneous OH-PLIF and PIV measurements in a gas turbine model combustor *Applied Physics B: Lasers and Optics* **90**(3) 609-618
25. Einecke S, Schulz C and Sick V 2000 Measurement of temperature, fuel concentration and equivalence ratio fields using tracer LIF in IC engine combustion *Applied Physics B: Lasers and Optics* **71** 717-723
26. Morin C, Modica V and Guibert P 2008 Measurement of exhaust gas recirculation rate by laser-induced fluorescence in engine *Measurement Science and Technology* **19** 1-11
27. Wolff M, Delconte A, Schmidt F, Gucher P and Lemoine F 2007 High-pressure diesel spray temperature measurements using two-colour laser-induced fluorescence *Measurement Science and Technology* **18** 697-706
28. Depredurand V, Miron P, Labergue A, Wolff M, Castanet G and Lemoine F 2008 A temperature-sensitive tracer suitable for two-colour laser-induced fluorescence thermometry applied to evaporating fuel droplets *Measurement Science and Technology* **19** 1-12
29. Luong M, Koban W and Schulz C 2005 Novel strategies for imaging temperature distribution using Toluene LIF *Second International Conference on Optical and Laser Diagnostics*
30. Luong M, Zhang R, Schulz C and Schulz C 2008 Toluene laser-induced fluorescence for in-cylinder temperature imaging in internal combustion engines *Applied Physics B: Lasers and Optics* **91** 669-675
31. Strozzi C, Sotton J, Mura A and Bellenoue M 2009 Characterization of a two-dimensional temperature field within a rapid compression machine using a toluene planar laser-induced fluorescence imaging technique *Measurement Science and Technology* **20** 1-13
32. Hu H, Saga T, Kobayashi T and Taniguchi N 2000 Research on the vortical and turbulent structures in the lobed jet flow using laser induced fluorescence and particle image velocimetry techniques *Measurement Science and Technology* **11** 698-711
33. Lachney E R and Clemens N T 1998 PLIF imaging of mean temperature and pressure in a supersonic bluff wake *Experiments in Fluids* **24** 354-363
34. Fuyuto T, Kronemayer H, Lewerich B, Koban W, Akihama K and Schulz C 2006 Laser-based temperature imaging close to surfaces with toluene and NO-LIF *Second International Conference on Optical and Laser Diagnostics (ICOLAD 2005)* Journal of Physics: Conference Series 45 69-76, Institute of Physics Publishing
35. Thurber M C, Grisch F and Hanson R K 1997 Temperature imaging with single-and dual-wavelength acetone planar laser-induced fluorescence *Optics Letters* **22**(4) 251-253
36. Thurber M C and Hanson R K 1999 Pressure and composition dependences of acetone laser-induced fluorescence with excitation at 248, 266, and 308 nm *Applied Physics B: Lasers and Optics* **69**(3) 229-240
37. Thurber M C and Hanson R K 2001 Simultaneous imaging of temperature and mole fraction using acetone planar laser-induced fluorescence *Experiments in Fluids* **30**(1) 93-101
38. Bresson A, Brossard C, Gicquel P and Grisch F 2003 Simultaneous temperature, concentration, and velocity fields

measurements in a turbulent heated jet using combined laser-induced fluorescence and PIV *Proceedings of SPIE* **5191** 75-86

39. Degardin O, Renou B and Boukhalfa A M 2006 Simultaneous measurement of temperature and fuel mole fraction using acetone planar induced fluorescence and Rayleigh scattering in stratified flames *Experiments in Fluids* **40** 452-463
40. Kearney S P and Reyes F V 2003 Quantitative temperature imaging in gas-phase turbulent thermal convection by laser-induced fluorescence of acetone *Experiments in Fluids* **34**(1) 87-97
41. Bryant R A, Donbar J M and Driscoll J F 1997 Acetone LIF for flow visualization at temperatures below 300 K *AIAA paper* 97-156
42. Bryant R A, Donbar J M and Driscoll J F 2000 Acetone laser induced fluorescence for low pressure/low temperature flow visualization *Experiments in Fluids* **28** 471-476
43. Lozano A, Yip B and Hanson R K 1992 Acetone: a tracer for concentration measurements in gaseous flows by planar laser-induced fluorescence *Experiments in Fluids* **13**(6) 369-376
44. Ritchie B D and Seitzman J M 2001 Quantitative acetone PLIF in two-phase flows *AIAA paper* **0414** 1-7
45. Miller M F, Bowman C T and Mungal M G 1998 An experimental investigation of the effects of compressibility on a turbulent reacting mixing layer *Journal of Fluid Mechanics* **356** 25-64
46. LaVision Product-Manual 2007
47. Mao X, Yu Z and Jaworski A J 2008 PIV studies of coherent structures generated at the end of a stack of parallel plates in a standing wave acoustic field *Experiments in Fluids* **45** 833-846
48. Wakeland R S and Keolian R M 2002 Thermoacoustics with idealized heat exchangers and no stack *The Journal of the Acoustical Society of America* **111**(6) 2654-2664
49. Heraeus company database of quartz glass (http://www.optics.heraeus-quarzglas.com)
50. Acetone MSDS 2007 (http://www.jtbaker.com/msds/englishhtml/A0446.htm)
51. Shi L, Yu Z and Jaworski A J 2009 PLIF measurement of instantaneous temperature field within thermoacoustic heat exchangers *Proc. Society for Experimental Mechanics - SEM Annual Conference and Exposition on Experimental and Applied Mechanics 2009*, **1** 221-230 (Albuquerque, New Mexico, USA)
52. Clemens N T 2002 *Flow imaging*, *Encyclopedia of Imaging Science and Technology*, John Wiley and Sons, New York
53. Paul P H, van Cruyningen I, Hanson R K, Kychakoff G 1990 High resolution digital flowfield imaging of jet *Experiments in Fluids* **9** 241-251
54. Abramenko, T N, Aleinikova V I, Golovicher L E and Kuzmina N E 1992 Generalization of experimental data on thermal conductivity of nitrogen, oxygen, and air at atmospheric pressure *Journal of Engineering Physics and Thermophysics* **63**(3) 892-897
55. Zhao T and Cheng P 1995 A numerical solution of laminar forced convection in a heated pipe subjected to a reciprocating flow *International Journal of Heat and Mass Transfer* **38**(16) 3011-3022
56. Bevington P R and Robinson D K 2002 *Data Reduction and Error Analysis for the Physical Sciences*, 3rd Ed. (McGraw-Hill)
57. Byrne S O, Danehy P M and Houwing A F P 2003 *PLIF temperature and velocity distributions in laminar hypersonic flat-plate flow*, 12th Gordon Research Conference on Laser Diagnostics for Combustion, 17-22 Aug. 2003, Oxford, United Kingdom
58. Palma P C, McIntyre T J and Houwing A F P 1998 PLIF thermometry in shock tunnel flows using a Raman-shifted tunable excimer laser *Shock Waves* **8** 275-284